Monthly Notices
of the
ROYAL ASTRONOMICAL SOCIETY

Mon. Not. R. Astron. Soc. **421,** 2094–2108 (2012) doi:10.1111/j.1365-2966.2012.20462.x

Asteroid rotation periods from the Palomar Transient Factory survey

D. Polishook,[1⋆] E. O. Ofek,[1] A. Waszczak,[2] S. R. Kulkarni,[2] A. Gal-Yam,[1] O. Aharonson,[1] R. Laher,[3] J. Surace,[3] C. Klein,[4] J. Bloom,[4] N. Brosch,[5] D. Prialnik,[5] C. Grillmair,[6] S. B. Cenko,[4] M. Kasliwal,[2] N. Law,[7] D. Levitan,[2] P. Nugent,[8] D. Poznanski[4,5,8]† and R. Quimby[2]

[1]*Benoziyo Center for Astrophysics, Weizmann Institute of Science, 76100 Rehovot, Israel*
[2]*Division of Physics, Mathematics and Astronomy, California Institute of Technology, Pasadena, CA 91125, USA*
[3]*Spitzer Science Center, California Institute of Technology, M/S 314-6, Pasadena, CA 91125, USA*
[4]*Department of Astronomy, University of California, Berkeley, CA 94720-3411, USA*
[5]*Faculty of Exact Sciences, Tel-Aviv University, 69978 Tel-Aviv-Yafo, Israel*
[6]*Infrared Processing and Analysis Center, California Institute of Technology, M/S 100-22, Pasadena, CA 91125, USA*
[7]*Dunlap Institute for Astronomy and Astrophysics, University of Toronto, Toronto, Ontario M5S 3H4, Canada*
[8]*Computational Cosmology Center, Lawrence Berkeley National Laboratory, Berkeley, CA 94720, USA*

Accepted 2011 December 23. Received 2011 December 22; in original form 2011 October 17

ABSTRACT

The Palomar Transient Factory (PTF) is a synoptic survey designed to explore the transient and variable sky in a wide variety of cadences. We use PTF observations of fields that were observed multiple times ($\gtrsim$10) per night, for several nights, to find asteroids, construct their light curves and measure their rotation periods. Here we describe the pipeline we use to achieve these goals and present the results from the first four (overlapping) PTF fields analysed as part of this programme. These fields, which cover an area of 21 deg^2, were observed on four nights with a cadence of $\sim$20 min. Our pipeline was able to detect 624 asteroids, of which 145 ($\approx$20 per cent) were previously unknown. We present high-quality rotation periods for 88 main-belt asteroids and possible period or lower limit on the period for an additional 85 asteroids. For the remaining 451 asteroids, we present lower limits on their photometric amplitudes. Three of the asteroids have light curves that are characteristic of binary asteroids. We estimate that implementing our search for all existing high-cadence PTF data will provide rotation periods for about 10 000 asteroids mainly in the magnitude range $\approx$14 to $\approx$20.

Key words: surveys – minor planets, asteroids: general.

1 INTRODUCTION

We can use time series photometry of asteroids and other types of minor planets to study a wide variety of their physical characteristics. The rotation period (spin) can be derived from periodicity in their light curves (e.g. Harris et al. 1989); the light-curve structure and changes in their mean amplitude as a function of viewing angle allow us to reconstruct their shapes (e.g. Kaasalainen & Torppa 2001); and it provides a method to search for binary asteroids (e.g. Polishook, Brosch & Prialnik 2011). In some cases, the presence of satellites allows the determination of the mass and/or density of the asteroids (e.g. Gnat & Sari 2010). Furthermore, and most relevant to our work, statistics of asteroid rotation periods can be used to understand the physical mechanisms that shape their rotation periods – presumably, the two main mechanisms involved are collisions (Davis et al. 2002) and the thermal Yarkovsky–O'Keefe–Radzievskii–Paddack (YORP) effect (Rubincam 2000).

To date, there are $\approx$3700 asteroids with published light curves and rotation periods (Warner, Harris & Pravec 2009). Rotation periods of asteroids are typically derived from multiple photometric observations of the same object taken on several nights. Significant contributions were made by amateur astronomers with modest equipment. In recent years, wide-field CCDs provide photometric measurements of many asteroids simultaneously, by dedicated surveys (e.g. Masiero et al. 2009; Polishook & Brosch 2009), or as part of multipurpose surveys, such as the Sloan Digital Sky Survey (SDSS; Ivezić et al. 2001; Ofek 2012). Observations using 1–2 m class telescopes can deliver the rotation periods for $\approx$1-km-size main-belt asteroids. Such small asteroids are particularly interesting since the time-scale of physical mechanisms, such as the YORP effect is relatively short, about 10^6 yr (Rubincam 2000; Vokrouhlický & Čapek 2002).

⋆E-mail: david.polishook@weizmann.ac.il
†Einstein fellow.

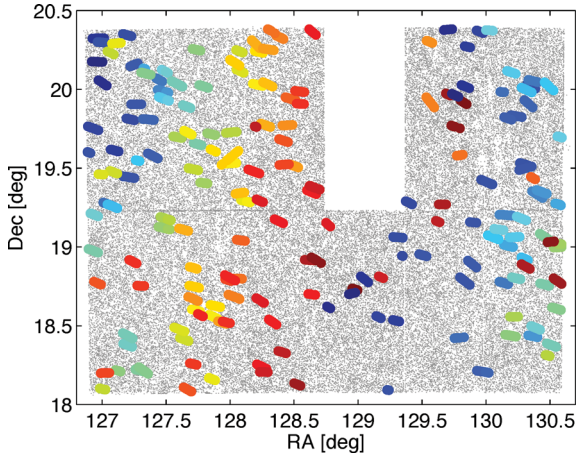

Figure 1. A single PTF field of view of $3.^{\circ}6 \times 2.^{\circ}3$. The coloured circles are the detected asteroids, while the grey dots represent stationary background sources. The missing rectangular area is due to a malfunctioning CCD. The data are based on observations of PTF field 110004 taken on 2010 February 14 (see Table 1).

Herein we describe a pipeline designed to detect asteroids, construct their light curves and measure their rotation periods, in data obtained by the Palomar Transient Factory (PTF;[1] Law et al. 2009; Rau et al. 2009). The PTF is an automated, wide-field survey aimed at a systematic exploration of the optical transient sky. Operating daily, the survey uses a camera with a 7.26 deg^2 field of view assembled on the 1.2-m Oschin telescope at Palomar Observatory (Rahmer et al. 2008). The camera is a mosaic of 11 CCDs, with pixel scale of 1.01 arcsec pixel^{-1} (e.g. Fig. 1). With an exposure time of 60 s the survey reaches a limiting magnitude of $\sim$21 mag with a median seeing of $\approx$2 arcsec. The two filters frequently used are Mould-R and SDSS-g'. The PTF survey samples the sky in a variety of cadences to match the scientific goals of different programmes, such as the search for supernovae (e.g. Arcavi et al. 2010) and galactic variables (e.g. Levitan et al. 2011). Part of the PTF time is used for high-cadence observations, in which we obtain $\gtrsim 20$ observations of the same field in a given night, and in some cases we repeat these high-cadence observations on multiple nights.

This paper is organized as follows. In Section 2 we describe the PTF asteroid pipeline. Section 3 presents the observations analysed in this study, while in Section 4 we give the results. Finally, we conclude in Section 5.

2 THE PTF ASTEROID PIPELINE

2.1 Asteroid identification

Each PTF image is processed by the IPAC-PTF[2] pipeline. The processing includes splitting the images, de-biasing, flat-fielding, astrometric calibration, preparation of mask images, source extraction and magnitude calibration. An overview of the IPAC-PTF pipeline may be found in Grillmair et al. (2010) and is described in detail by Laher et al. (in preparation). The photometric calibration is discussed in Ofek et al. (2012). The mask images contain information about bad pixels, probable optical ghosts, saturated pixels, aircraft/satellite tracks and more. The source detection and extraction is performed using SExtractor (Bertin & Arnouts 1996). Here we use the SExtractor MAG_AUTO magnitudes[3] (see Kron 1980). However, our experience is that the MAG_AUTO magnitudes are slightly biased for objects fainter than 19 mag (Ofek et al. 2012). In the future we plan to use aperture magnitude. The processed images and their associated catalogue files are analysed using the MATLAB-based PTF/asteroids rotation pipeline described below.

Detection of moving sources is done on a per-field and per-CCD basis in catalogue space. For each PTF field/CCD, we construct a reference image based on about 10 images with the best seeing values [lowest full width at half-maximum (FWHM) and lowest background]. Then we use SExtractor to detect the sources in the reference image. We match all the sources with 2 arcsec matching radius in each one of the individual epochs against the reference image catalogue. Matching sources against the reference catalogue, rather than against one of the epochs, is done for two important reasons: (i) the moving sources do not appear in the reference catalogue and (ii) the deep reference catalogue contains almost all of the stationary sources because faint static sources which are just at, or below, the level of the background noise for a specific image will co-ad to be detected in the reference image. Therefore, even if these stationary sources are detected in only a few of the individual images they will not be mistaken as moving sources.

The sources from each science image that do not appear in the reference catalogue are considered as moving source candidates. However, a large fraction of these candidates are cosmic rays, artefacts or spurious detections. A significant part of the artefacts appears in haloes around saturated stars and on pixels created by blooming. We identify these sources by their proximity to stars brighter than 11th mag (the Tycho-2 catalogue is used as a reference; Høg et al. 2000) and reject them from the list of candidates.

Next, we associate moving source candidates which are detections of the same physical object – we call these 'tracks'. Tracks are constructed using the following algorithm: for the ith candidate in the jth image, the software searches for a second appearance in the $j+1$ image (the images are sorted by time). The search radius is $v_{\rm max}(t_{j+1} - t_j)$, where t_j is the time of the j image and $v_{\rm max}$ is the maximum speed specified by the user.[4] Here, we use $v_{\rm max} = 0.25$ arcsec s^{-1}. We note that it is possible to have more than one candidate within the search radius in the $j+1$ image. Therefore, we treat each candidate source in the $j+1$ image as a possible detection of the object in the sequence. For each such possible track we look for another source in the $j+2$ image. The search is done by looking for a source around a position:

$$\alpha_{j+2} = \alpha_{j+1} + \frac{\alpha_{j+1} - \alpha_j}{t_{j+1} - t_j}(t_{j+2} - t_{j+1}), \quad (1)$$

$$\delta_{j+2} = \delta_{j+1} + \frac{\delta_{j+1} - \delta_j}{t_{j+1} - t_j}(t_{j+2} - t_{j+1}). \quad (2)$$

Here α and δ are the right ascension and the declination of the object, respectively, and the subscripts indicate the image index. The search radius, ΔR, around this location is

$$\Delta R = \max(\Delta\alpha_{j+2}, \Delta\delta_{j+2}) + 2\,\text{arcsec}, \quad (3)$$

[1] http://www.astro.caltech.edu/ptf/
[2] Infrared Processing and Analysis Center: http://www.ipac.caltech.edu/

[3] Defined with kron_fact = 1.5 and min_radius = 2.5.
[4] Main belt asteroids have typical angular speeds of $\sim$0.01 arcsec s^{-1}, while near-Earth asteroids can move at a rate of $\sim$0.1 arcsec s^{-1} and trans-Neptunian objects have a slow motion of order 0.001 arcsec s^{-1}.

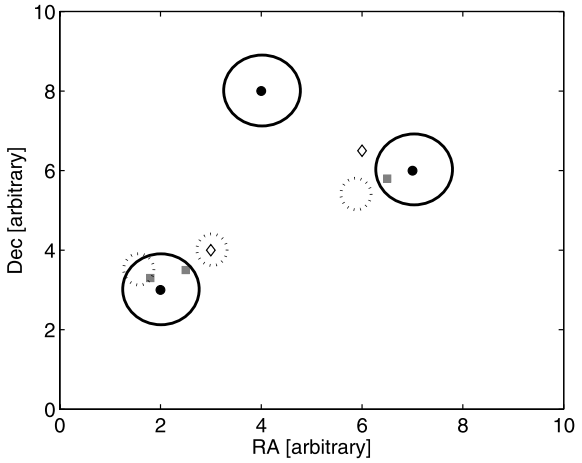

Figure 2. Illustration of the track detection algorithm. All symbols are sources that do not appear in the reference image and, therefore, they are treated as moving source candidates. The three black-filled circles appear in the first image. The program searches for candidates in the second image within a radius determined by the user and marked here by empty circles. If a candidate is found in the second image (grey squares), we search for a candidate in the third image (empty diamonds). The search region in the third image (marked by dashed circles) is calculated by equation (3). In the case presented here only one asteroid will be detected by the code (i.e. bottom left).

where

$$\Delta\alpha_{j+2} = \sqrt{\Delta\alpha_{j+1}^2 + \frac{\Delta\alpha_{j+1}^2 + \Delta\alpha_j^2}{(t_{j+1} - t_j)^2}(t_{j+2} - t_{j+1})^2}, \quad (4)$$

$$\Delta\delta_{j+2} = \sqrt{\Delta\delta_{j+1}^2 + \frac{\Delta\delta_{j+1}^2 + \Delta\delta_j^2}{(t_{j+1} - t_j)^2}(t_{j+2} - t_{j+1})^2}. \quad (5)$$

Here $\Delta\alpha$ and $\Delta\delta$ are the astrometric errors[5] in the right ascension and declination, respectively. 2 arcsec is a constant matching radius added in order to avoid problems due to underestimation of the astrometric errors and any deviations from linear motion of the objects. As a result, moving sources that have a total motion of less than 2 arcsec in the scanned set of images could not be detected. The search for additional sources associated with each possible track continues recursively on following images, until the moving source does not appear in the $j + n$ image. In the case a single source in the first image is branching to multiple possible tracks, our recursive algorithm calculates all the possible tracks and selects the longest track (i.e. the one that contains the greatest number of points) as the most likely track. The sources that belong to this most likely track are flagged as 'associated with a track' and the algorithm keeps running on all the sources which are not associated with a track until it runs out of sources or until the sources that remain unassociated cannot be matched. For clarity, the algorithm is visually presented in Fig. 2. After scanning all the images, each track is fitted with a second-order polynomial in right ascension and declination using linear least squares, and the χ^2 and degrees of freedom for each fit are stored along with the track's properties.

Since the current version of the algorithm requires an asteroid to appear in successive images, it can identify multiple tracks that, in fact, belong to the same asteroid. This is possible when a moving source is not identified in one of the epochs and this may happen, for example, when the asteroid is blended with a star, or if its signal-to-noise ratio is too low in a specific image. Therefore, next we try to merge all the tracks that belong to the same moving object. This is done by fitting the points of any pair of tracks that were observed in the same night, field and CCD to a second order polynomial. Tracks are merged if the χ^2 of the fit is less than a predefined value. Similarly, single 'orphan' sources (i.e. sources that do not appear in the reference catalogue and were rejected by the detection code in previous steps) are tested as additional points belonging to the detected tracks.

Some of the tracks, especially those containing a small number of points, or those that are very short (i.e. due to small angular speed) may be artefacts and not real astrophysical sources. Another type of false alarm is created by pixels on blooming columns of saturated bright stars that were not flagged by the code in a previous stage and are mistakenly considered as sources by SExtractor. These 'objects' have a unique trajectory (i.e. a nearly north-to-south or south-to-north motion) and have similar right ascension values to stars brighter than ∼11 mag (here also we use the Tycho-2 catalogue; Høg et al. 2000). All the unknown detections not marked by the pipeline as false alarms are manually scanned to test their validity. While this manual scan is a simple and fast process, we wish to cancel this step by matching better thresholds to the data and make it completely automatic.

The data collected for each moving source include its position, time, angular velocity (projected into the image data), exposure parameters, χ^2, number of degrees of freedom and instrumental magnitudes measured by SExtractor. Saving these values becomes handy for the remaining steps of the procedure. The detected moving sources are identified by the PyMPChecker web service.[6] This tool provides asteroid positions around a sky and time coordinates. In addition, all the objects receive an internal PTF designation which is a running number in base 36 (digits + letters). The measured coordinates and photometry are reported to the Minor Planet Center.[7]

Asteroids observed on different nights, fields and CCDs are combined into a single track. The identification of different sources as belonging to the same asteroid is done according to the designations of the known objects. If an object is unknown, we fit a second-order polynomial to all the possible track combinations and merge tracks which are consistent with being due to a single moving source. While this method of track merging is limited to data from successive nights, it is sufficient for our purpose of spin analysis.

2.2 Photometric calibration

In order to construct the best relative photometry light curve of each source we use a linear-least-squares minimization technique, in which we solve for the best zero-point normalization (per epoch), and the best 'mean' flux density of each source that minimize the global scatter in all the light curves of stationary sources. Furthermore, using a set of linear constraints on the magnitudes of some of the reference stars, we simultaneously calibrate the magnitude to an absolute scale using the *r*-band magnitude of SDSS stars (York et al. 2000). This technique was introduced by Honeycutt (1992), with some modifications and the simultaneous absolute calibration presented in Ofek et al. (2012). We note that PTF data routinely

[5] The astrometric errors are taken from the square of the SExtractor parameters ERRX2WIN_IMAGE and ERRY2WIN_IMAGE.

[6] http://dotastro.org/PyMPC/PyMPC/

[7] http://minorplanetcenter.net/

achieve relative photometry accuracy of as good as 3 mmag (e.g. Agüeros et al. 2011; Levitan et al. 2011; van Eyken et al. 2011).

We perform the calibration process for each night and each CCD separately. However, some asteroids are visible on multiple nights and/or multiple CCDs. Therefore, the absolute photometric accuracy of SDSS magnitudes (20 mmag) and CCD diversity may introduce a small systematic offset between light curves of the same asteroid observed on multiple nights and/or multiple CCDs. We correct for these effects during the period fitting process described in Section 2.3.

Each moving source is saved with its instrumental magnitude and zero-point, for each image. Following the photometric calibration step, the observing times are corrected for light-travel time and the calibrated magnitudes ($R_{\rm PTF}$) are reduced to geocentric (r) and heliocentric (Δ) distances of 1 au using

$$M_{(r=1,\Delta=1)} = R_{\rm PTF} + 5\log(r\Delta). \quad (6)$$

The mean calibrated magnitude ($\langle R_{\rm PTF}\rangle$), phase angle ($\alpha$), geocentric ($r$) and heliocentric ($\Delta$) distances of the detected asteroids are presented in Tables 2–5. This correction is done only for objects with known orbital parameters.

We do not try to fit the data to a *H–G* system (i.e. the coefficients that describe the brightness decrease with increasing phase angle), since the phase angles of the observed asteroids change only slightly over the 4-d observing period. Instead, we estimate the absolute magnitude H using a fixed G slope of 0.15 and using (Bowell et al. 1989)

$$H = \langle M_{(r=1,\Delta=1)}\rangle + 2.5\log[(1-G)\phi_1 + G\phi_2], \quad (7)$$

where

$$\phi_1 = \exp(-3.33\tan(0.5\langle\alpha\rangle)^{0.63}), \quad (8)$$

$$\phi_2 = \exp(-1.87\tan(0.5\langle\alpha\rangle)^{1.22}). \quad (9)$$

2.3 Rotation period analysis

In order to find the synodic rotation period of the asteroids, we fit a second-order Fourier series to each light curve of a merged track:

$$M_j = \sum_{k=1,2}^{N_k} B_k \sin\left[\frac{2\pi k}{P}(t_j - t_0)\right] + C_k \cos\left[\frac{2\pi k}{P}(t_j - t_0)\right] + \sum_{s=1}^{N_s} Z_s, \quad (10)$$

where B_k and C_k are the Fourier coefficients, P is the rotation period, M_j is the photometric data at t_j (after the reduction to absolute planetary magnitude; i.e. equation 6) and t_0 is an arbitrary epoch. As described in Section 2.2, photometric calibration is performed separately for each set of images taken at different nights and/or CCDs. Therefore, in order to improve the photometric calibration, we also fit in equation (10) a constant value (Z_s) for each set of images, where a set (s) is defined as all the measurements taken on the same night, field and CCD. N_s is the number of sets. For a given P, this yields a set of linear equations which is solved using least-squares minimization to obtain the free parameters. This calculation is performed for a set of trial frequencies ranging from the Nyquist frequency to one over the total time span of the light curve, and in steps of 0.25 divided by the time span of the light curve (i.e. oversampling of 4). The typical trial periods range from about 20 min to about 80 h, which cover the rotation periods of most asteroids (e.g. Pravec & Harris 2000).

The frequency with the minimal χ^2 is chosen as the most likely period. The error in the best-fitting frequency is determined by the range of periods with χ^2 smaller than the minimum $\chi^2 + \Delta\chi^2$, where $\Delta\chi^2$ is calculated from the inverse χ^2 distribution assuming $1 + 2N_k + N_s$ degrees of freedom. The code automatically rejects cases in which there are multiple solutions; cases where the best match is at the edge of the tested period range; or if only a few measurements exist (i.e. <8 data points). All the other matches are manually scanned to test the validity of their period and folded light curve. Light curves which show two peaks with photometric errors that are smaller than the light-curve amplitude and features repeating during different nights are considered as good quality light curves for which a periodicity can be derived. Poor results include cases where the light curve is folded on the photometric noise, giving usually short periods of around 20–30 min, which is the approximate sampling rate.

The folded light curves receive a reliability code based on the definitions of Warner et al. (2009), which are '3' for a highly reliable result with full light-curve coverage; '2' for an ambiguous result based on less than full coverage hence the result may be wrong by an integer ratio and '1' for periods that are based on fragmentary or noisy light curves that may be completely wrong. Only periods with a reliability code of 2 or 3 are used in statistical studies of asteroid rotations. Light curves that contain fragmentary data with no repeating features cannot be folded. However, some of these can be used to set lower limits on the rotation periods. These limits are determined from data that show a continuous and convincing magnitude variability (the amplitude is larger than the photometric error) from a single night/CCD set that is the longest in time.

We give lower limits on the amplitude of the light curves of all detected asteroids. This amplitude is based on 90 per cent of the magnitude range, Δm, centred on the range median (i.e. rejecting the upper and lower 5 per cent of the data). This is done to avoid photometric measurements which are contaminated by nearby sources or artefacts. Since data from different night/CCD sets might have small differences in their photometric calibration, we calculate the amplitude, $A_{\rm min}$, separately for each night/CCD set using

$$A_{\rm min} = \sqrt{\Delta m^2 - \langle\delta m\rangle^2}, \quad (11)$$

where $\langle\delta m\rangle$ is the average photometric error. We list the median value from all the sets as the lower limit on the amplitude. We note that light curves with low limits on the amplitudes belong to asteroids that rotate slowly or asteroids with a nearly circular projected shape.

2.4 Caveats and future improvements

The current algorithm misses some of the fainter asteroids. This is demonstrated in Fig. 3 where the peak of the magnitude distribution of the detected asteroids is at brighter magnitudes than the PTF detection limit. We are able to find more moving sources, which our search algorithm failed to find, using image blinking. One of the disadvantages of the current algorithm is that, unlike MOPS-like algorithms (e.g. Grav et al. 2011), it is not searching for tracks in all possible combinations of images and that it requires the object to appear in at least three successive images.

This disadvantage is not critical for the main application presented in this paper – rotation period measurements. This is because good photometry is available only for sources which are about 1 mag brighter than the detection limit. Such sources are rarely missed by our algorithm.

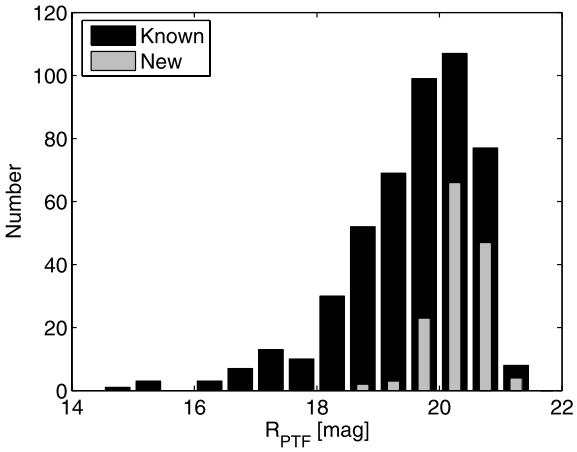

Figure 3. The distribution of magnitudes of known (black) and new (grey) asteroids found on this pilot run of the PTF survey. More than one-third of the asteroids fainter than 20 mag have not yet been discovered.

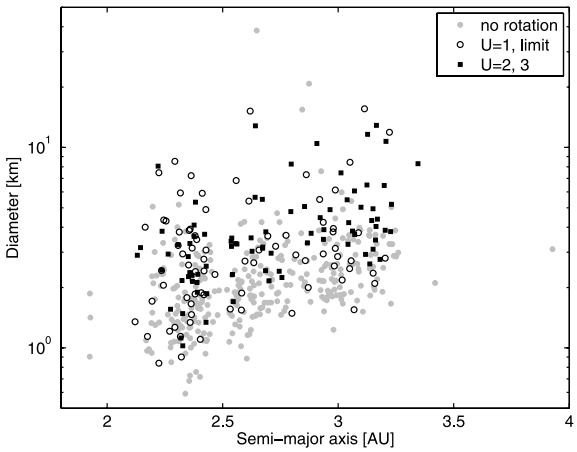

Figure 5. The estimated diameters of the known observed asteroids as a function of their semimajor axis a. Main-belt asteroids as small as 600 m are seen in this sample. A few bodies from the Hungaria group can be seen at $a < 2$ au. The gap at $a = 2.5$ au is the 1:3 Kirkwood gap.

3 OBSERVATIONS

We analyse PTF R-band images of four fields observed on four consecutive nights. The PTF field numbers as well as the observing dates are listed in Table 1. The four fields partially overlap (see Fig. 4) and cover a total area of 21 deg^2. The footprints of these fields cover ecliptic latitudes between $-0.^\circ75$ and $+2.^\circ5$. Table 1 also lists the total number of exposures taken on each night and the time duration of the observing period for acquiring each set of exposures for a given night and field. The seeing in the images ranged between 2.1 and 2.5 arcsec. We note that the observed fields are centred on the open cluster M44, and are also used by Agüeros et al. (2011) to study the mass–period relation of late-K to mid-M stars.

Table 1. Observed fields.

FIELD ID	RA (°)	Dec. (°)	Feb 12 N_{exp}, Δt	Feb 13 N_{exp}, Δt	Feb 14 N_{exp}, Δt	Feb 15 N_{exp}, Δt
110001	128.75	+19.25	23, 6.87	20, 8.57	29, 8.65	29, 8.70
110002	128.75	+20.24	23, 6.87	19, 8.58	29, 8.65	29, 8.74
110003	131.00	+19.25	23, 6.87	20, 8.88	29, 8.69	29, 8.74
110004	131.00	+20.24	23, 6.87	20, 8.88	29, 8.69	28, 8.78

Note. FIELD ID is a unique number representing PTF fields. N_{exp} is the number of exposures per night and field and Δt is the duration of time spanned by each set of observations, in hours. All observations were taken on 2010.

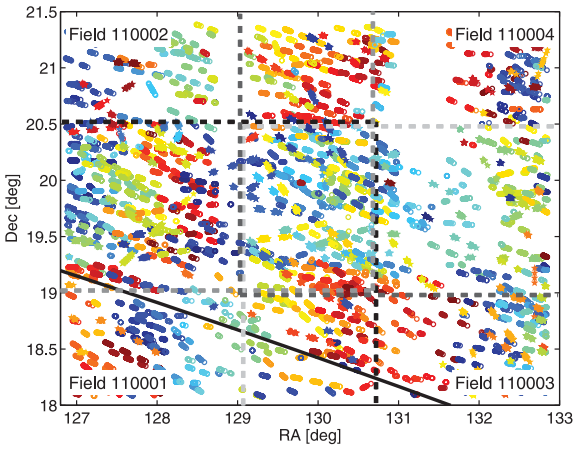

Figure 4. The tracks of 624 asteroids detected in the four overlapping fields listed in Table 1 (marked by the dashed lines). Coloured circles and pentagons are known and new asteroids, respectively. The black solid line represents the ecliptic.

4 RESULTS

4.1 Detected asteroids

We use the aforementioned asteroid pipeline to analyse the small set of PTF observations listed in Table 1. Running the algorithm described in Section 2.1 we found 624 asteroids of which 145 were not yet designated by the Minor Planet Center web service. Fig. 4 shows the tracks of all 624 detected asteroids within the field of view. The 145 unknown asteroids are fainter than 18.8 mag. The magnitude distribution, presented in Fig. 3, shows that more than a third of the asteroids with magnitude between 20 and 21 had not yet been discovered, while most (91 per cent) of the asteroids brighter than 20 are known.

The observed asteroids are located throughout the entire main-belt of asteroids, and spread out to about 4 au. A few members of the Hungaria group were also detected. Fig. 5 presents the diameters[8] of the observed asteroids, estimated assuming a geometric albedo[9] of 0.15, as a function of their semimajor axis a. The plot shows that the PTF survey can detect asteroids with diameters of hundreds of metres within the inner main belt ($a < 2.5$ au), and 1-km-size bodies in the outer main belt.

[8] Diameters are estimated using the formula

$$D = \frac{1329}{\sqrt{Pv}} 10^{-0.2H}, \quad (12)$$

where Pv is the geometric albedo and H is the absolute magnitude defined as the brightness of an asteroid at opposition with heliocentric and geocentric distances at 1 au. The estimated error of the diameters is less than a factor of 2, based on a statistical error of 0.12 for G (Lagerkvist & Magnusson 1990) and 0.1 for the albedo.

[9] The geometric albedo in visible light of main belt asteroids ranges from ≈0.05 to ≈0.4.

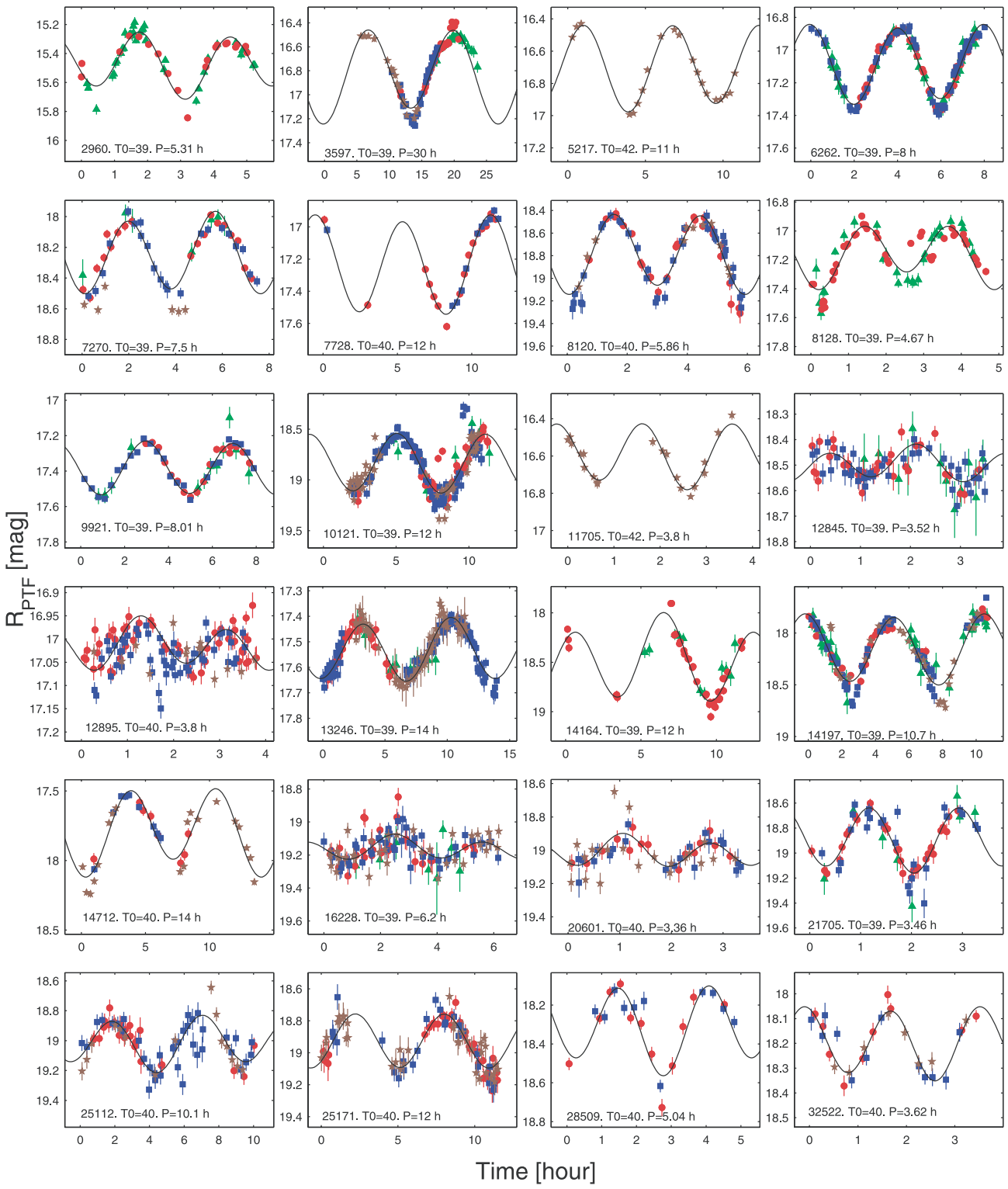

Figure 6. Set of 24 folded light curves. Reference epoch is $T_0 + 245\,5200$. Different markers indicate the observation date: 2010 February 12 – green triangles; 2010 February 13 – red circles; 2010 February 14 – blue squares; 2010 February 15 – brown pentagons. The designation of each asteroid, T_0 and the synodic rotation period P are given at the bottom of each plot.

4.2 Derived rotation periods

We were able to derive the rotation periods for 88 asteroids, with high reliability (codes 2 and 3), and, heretofore, none of these has a published light curve. The folded light curves are presented in Figs 6–9. The light curves of 85 objects with possible rotation periods and limits on the rotation period are presented in Figs 10 and 11, respectively. Four of these objects have published spin

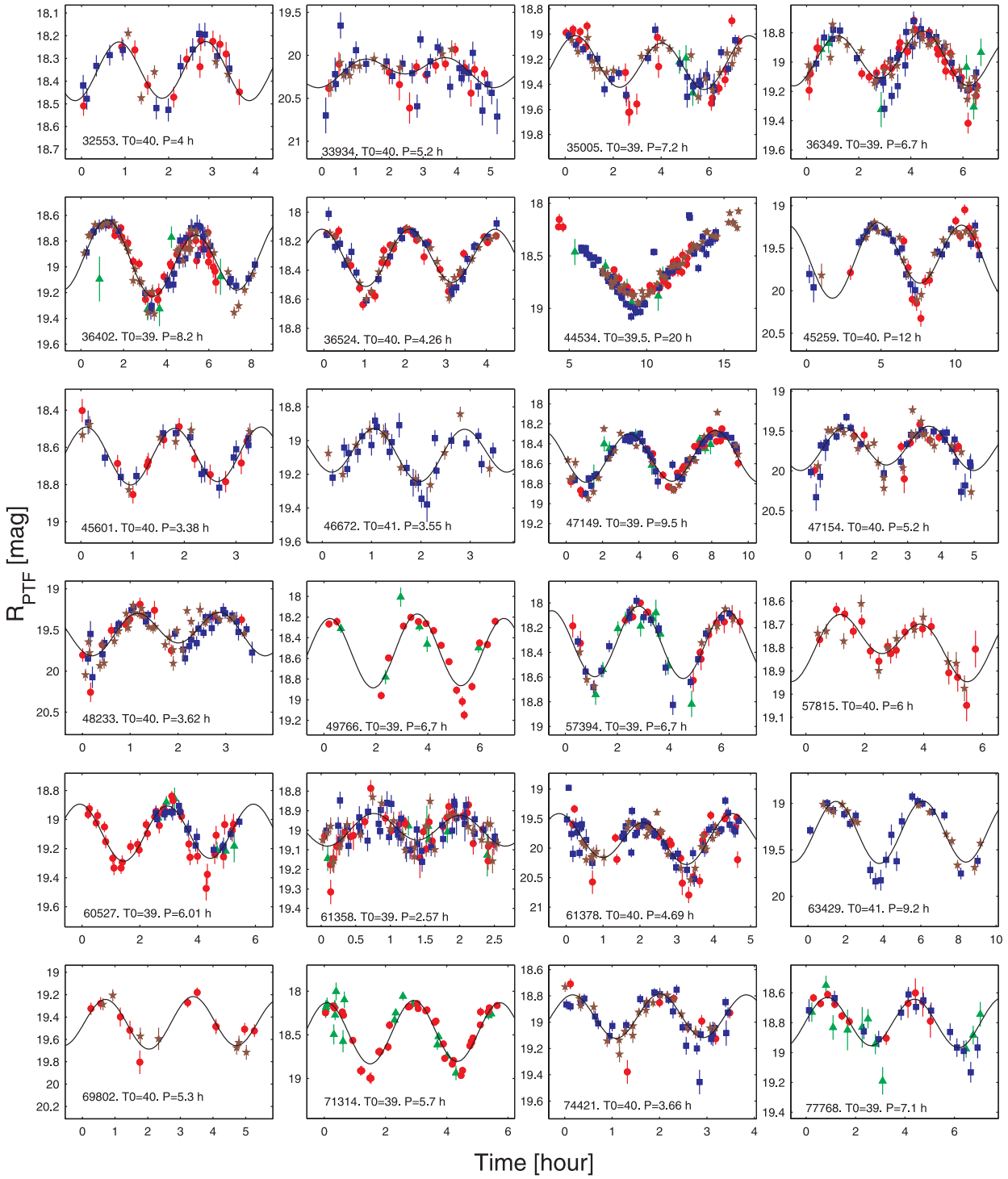

Figure 7. Same as Fig. 6 for 24 additional asteroids.

values, all are larger than the limit on the spin we present here.[10] The rotation periods and amplitudes with high reliability for 88 asteroids are summarized in Table 2. The possible rotation periods of 18 asteroids are shown in Table 3, while the lower limits on the rotation periods of 67 asteroids are listed in Table 4. We also provide lower limits on the amplitude of the rest of the detected asteroids in Table 5. Table 6 lists all of the measurements taken for the entire set of 624 detected asteroids.

Since most of the asteroids were observed during all four nights, where the total time-span between the first and the last images taken was about 80 h, this gives us an opportunity to detect rotations as

[10] These four asteroids with their already published rotation periods are 1516 Henry – 17.37 h, 6192 1990 KB1 – 11.1 h (both at http://obswww.unige.ch/~behrend/page_cou.html), 10207 Comeniana – 12.84 h (Galad, Kornos & Gajdos 2009), 23971 1998 YU9 – 6.8949 h (http://www.asu.cas.cz/~ppravec/neo.htm).

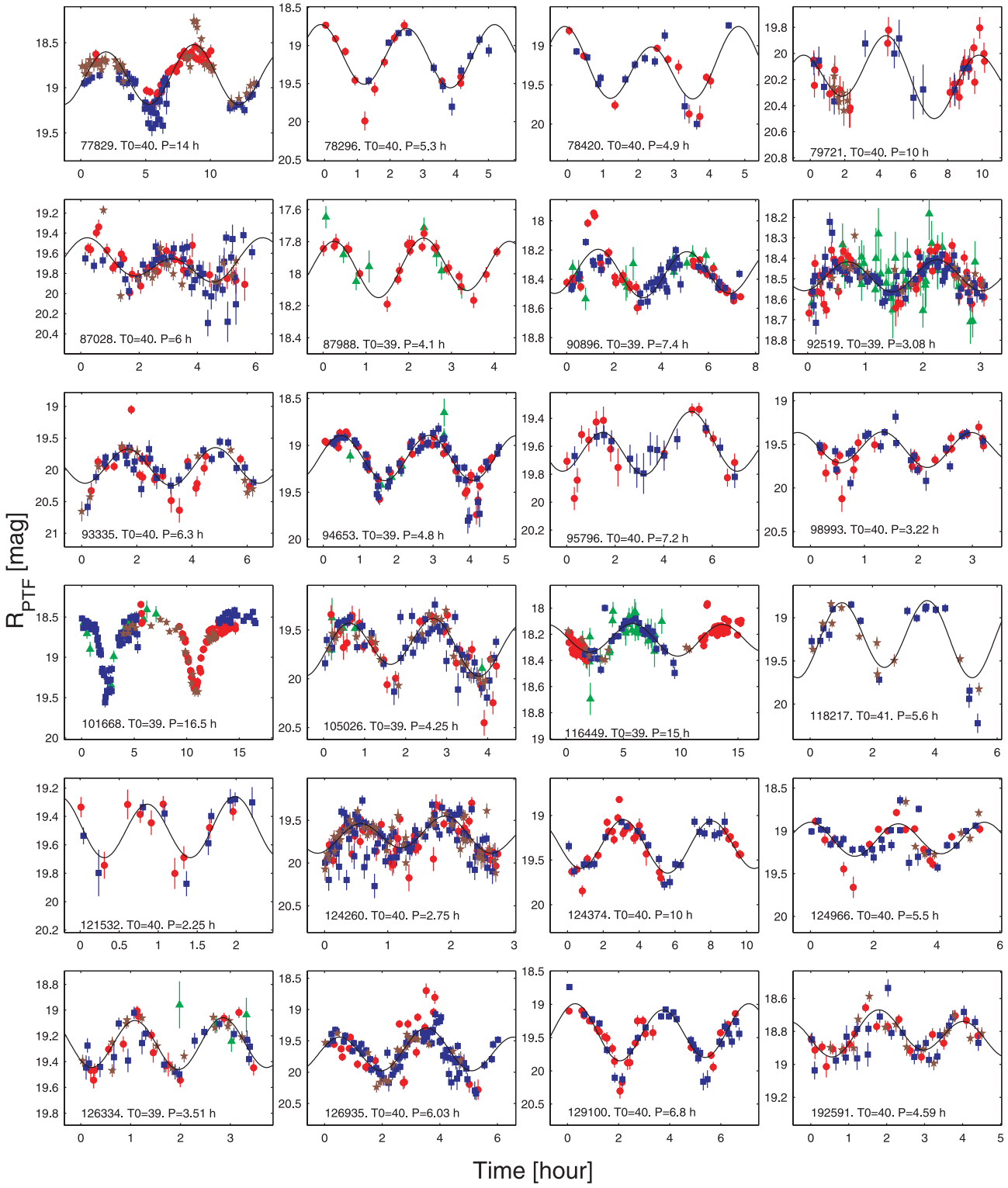

Figure 8. Same as Figs 6 and 7 for 24 additional asteroids. The deep V-shaped minima and the inverted-U-shaped maxima of asteroid (101668) 1999 CR95 suggest a binary nature.

slow as tens of hours. Since the field of view was observed during the entire night over the course of four consecutive nights, most asteroids in our survey were observed for a total of about 32 h (Table 1). Some of the asteroids were observed for shorter times due to poor weather conditions (especially on February 12) or because they were not within the field footprints in all four nights.

Among the light curves, three have features that are common among binary asteroids (Pravec et al. 2006). These features are deep V-shaped minima and wide inverted-U-shaped maxima. The deep V-shaped minima presumably represent a mutual event of eclipse or occultation between the primary and the secondary components. The three asteroids associated with the three aforementioned light

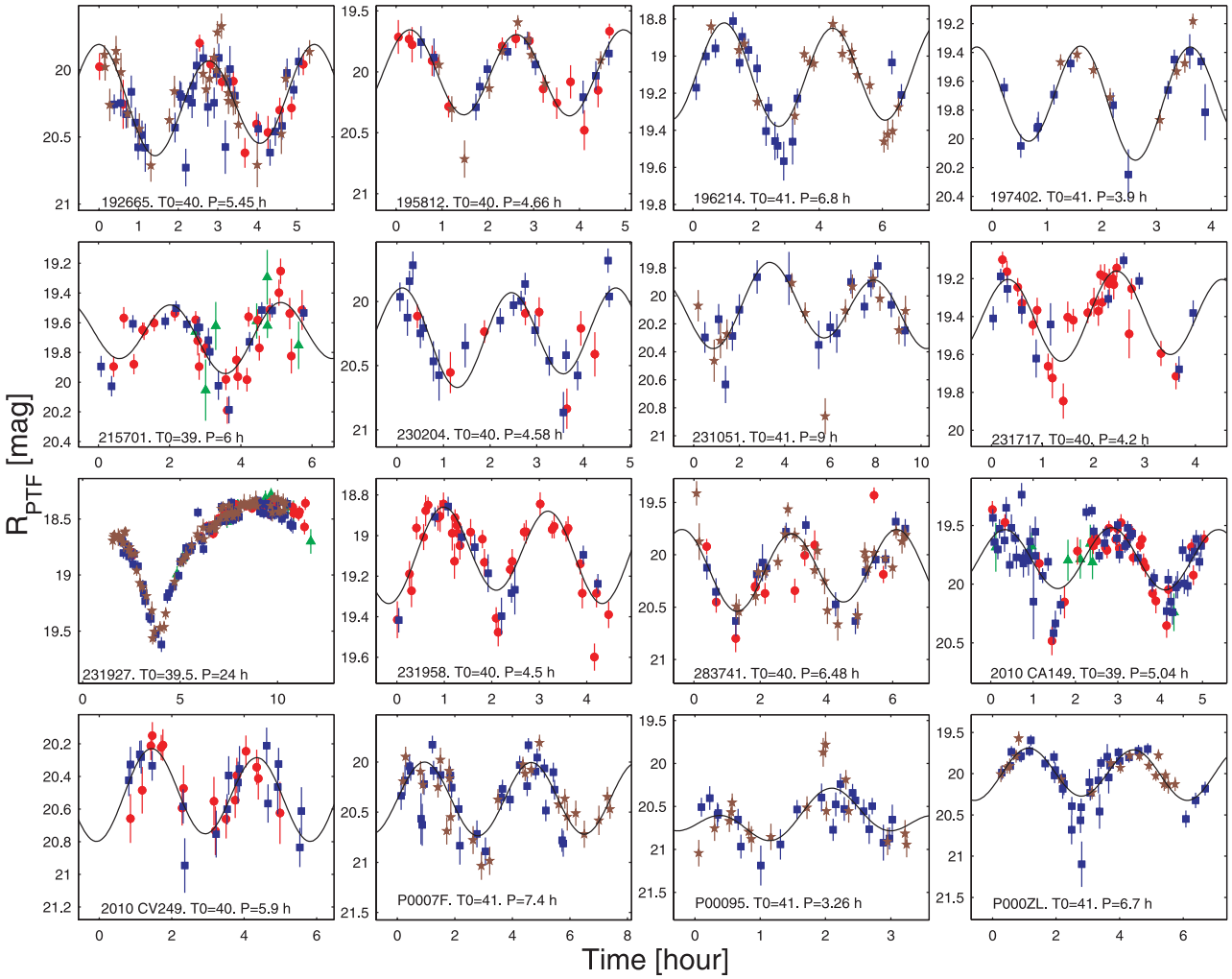

Figure 9. Same as Figs 6–8 for 16 additional asteroids. The deep V-shaped minima and the inverted-U-shaped maxima of asteroid (231927) 2001 DU30 suggest a binary nature.

curves are (17293) 2743 P-L (Fig. 10), (101668) 1999 CR95 (Fig. 8) and (231927) 2001 DU30 (Fig. 9). We note that there are some inconsistencies in the shape of the light curve of (17293) 2743 P-L as seen on different nights. If our estimated period is valid, then this may be the result of a non-spherical shape of one of the rotating components imposed on the brightness attenuation from the mutual event. The binary nature of these three objects should be confirmed with follow-up observations. If the features in these light curves are indeed due to mutual events of binary asteroids, then the periods reported here are the orbital periods of the components about their centre of mass, and the minima depth represents the approximate ratio between the diameters of the components.

5 SUMMARY AND FUTURE PROSPECTS

We present a pipeline that finds asteroids, constructs their light curves, and measures their rotation periods using images acquired by the PTF survey. We demonstrate our pipeline performance using a small sample of PTF data consisting of observations of about 21 deg^2 obtained over four nights with a cadence of ∼20 min. Within these images, we find 624 asteroids, of which 145 (≅20 per cent) were previously unknown. This shows that PTF is an efficient survey for studying known, as well as unknown asteroids. Among the new discoveries, many are small, km-sized objects. These may reveal the orbits of physically interesting objects such as small members of dynamical families (Bendjoya & Zappalà 2002) and secondary members of rotationally disintegrated objects (known as *asteroid pairs*; Vokrouhlický & Nesvorný 2008).

We obtain from our analysis high quality rotation periods for 88 main-belt asteroids and additional possible periods for 85 other asteroids. Based on the ecliptic latitude distribution of PTF high-cadence observations and our success rate in measuring asteroid periodicities, we roughly estimate that PTF can measure the rotation periods for about 10 000 asteroids. This large sample could be used to study the effects of different physical mechanisms on the spin evolution of asteroids. These mechanisms, such as collisions, the thermal YORP effect and tidal forces that follow planetary encounters, leave different signatures on the spin distribution of asteroids. For example, collisions generate a Maxwellian spin-rate distribution, as can be seen for large asteroids (>40 km; Pravec & Harris 2000), while the YORP effect creates a flatter spin-rate distribution (Pravec et al. 2008). A large PTF sample of asteroid rotation periods also could be used to compare the rotations of asteroids in different size groups and dynamical families (e.g. Polishook & Brosch 2009), and to track the rotational history of components ejected from rotationally disintegrated asteroids (Pravec et al. 2010).

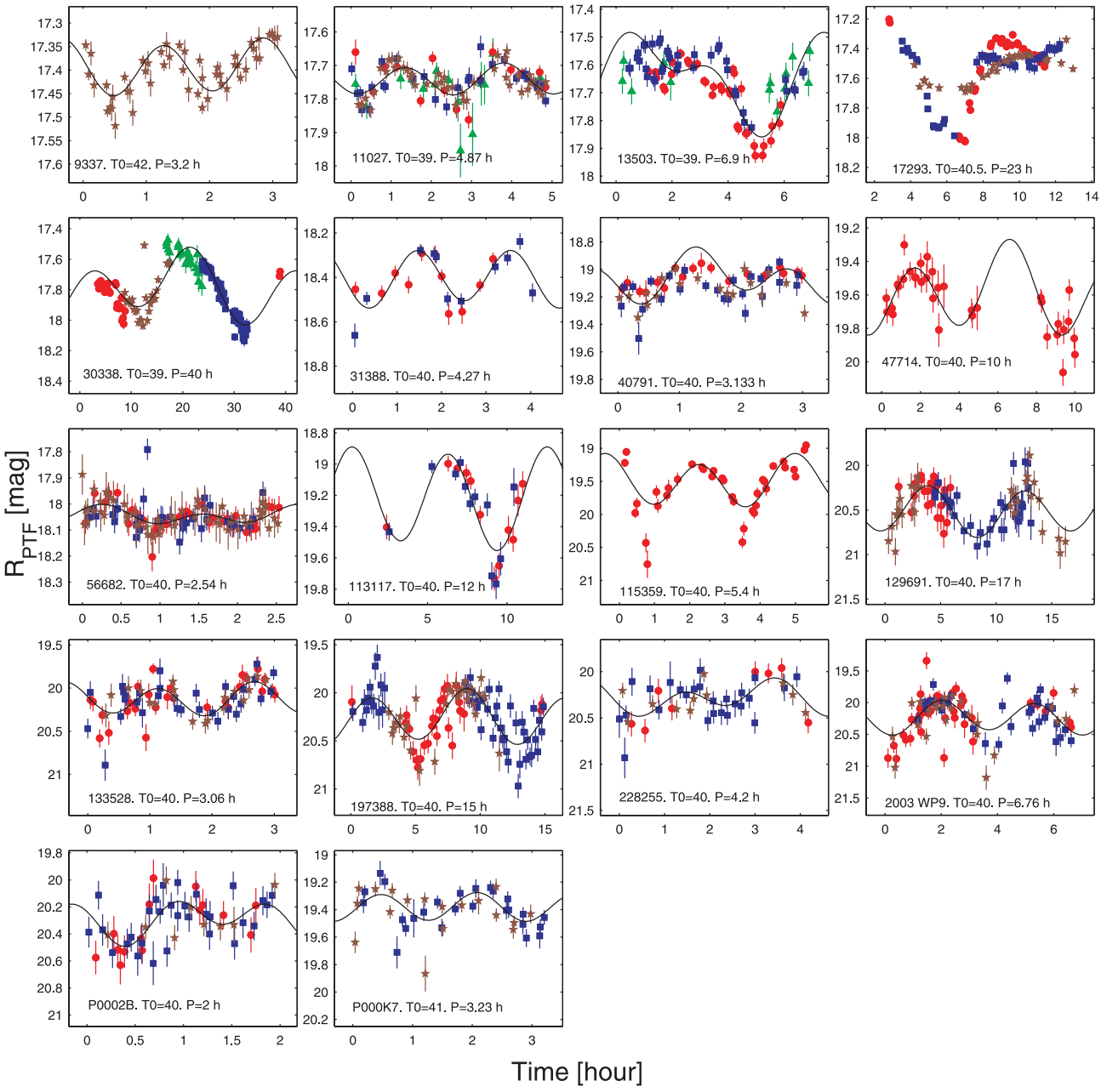

Figure 10. Set of 18 folded light curves with uncertain rotation periods ($U = 1$). See Fig. 6 for symbols description. The deep V-shaped minima of asteroid (17293) 2743 P-L and the inconsistency of the peak's shape between different nights suggest a binary nature.

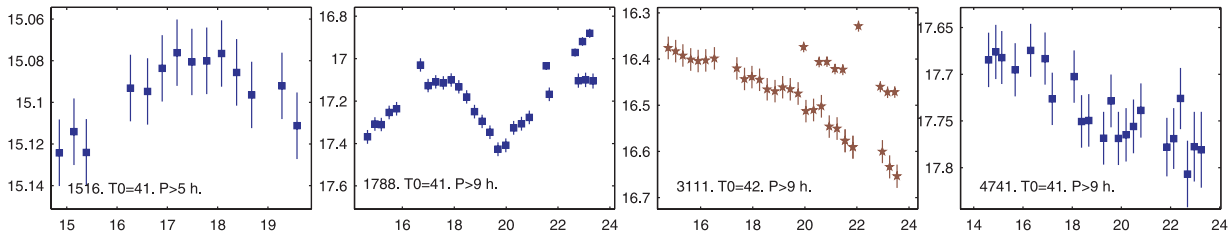

Figure 11. Set of four light curves with lower limits on the rotation periods. We only present data that show a continuous and convincing magnitude variability (the amplitude is larger than the photometric error) from a single night/CCD set that is the longest in time. See Fig. 6 for symbols description. This figure is published in its entirety as Supporting Information with the electronic version of the article. A portion of the full figure is shown here for guidance regarding its form and content.

Table 2. Synodic rotation periods of 88 asteroids with high reliability.

Designation	$N_{\rm nights}$	$N_{\rm im}$	r (au)	Δ (au)	α (°)	Period (h)	U	Amp (mag)	$\langle R_{\rm PTF}\rangle$ (mag)	a (au)
(2960) Ohtaki	2	57	2	1.03	8.1	5.31 ± 0.03	3	$\gtrsim 0.37$	15.42 ± 0.02	2.22
(3597) Kakkuri	4	97	3.23	2.28	5.6	27 ± 0.5	2	$\gtrsim 0.58$	16.78 ± 0.03	3.17
(5217) Chaozhou	1	20	2.3	1.33	7.1	11.3 ± 0.6	2	$\gtrsim 0.56$	16.73 ± 0.01	2.38
(6262) Javid	3	155	3.01	2.05	5.7	8.02 ± 0.05	3	$\gtrsim 0.45$	17.11 ± 0.03	2.91
(7270) Punkin	4	56	3.79	2.84	4.8	7.51 ± 0.07	3	$\gtrsim 0.5$	18.25 ± 0.04	3.21
(7728) Giblin	2	27	3.02	2.06	5.1	11.8 ± 0.3	2	$\gtrsim 0.61$	17.18 ± 0.02	2.8
(8120) Kobe	3	79	2.76	1.81	6.8	5.86 ± 0.04	3	$\gtrsim 0.74$	18.8 ± 0.05	2.42
(8128) Nicomachus	2	74	3.13	2.17	5.3	4.67 ± 0.02	3	$\gtrsim 0.54$	17.19 ± 0.03	3.13
(9921) 1981 EO18	3	55	2.33	1.36	6.2	8.01 ± 0.03	3	$\gtrsim 0.33$	17.37 ± 0.02	2.38
(10121) Arzamas	4	192	3.67	2.72	4.7	12.1 ± 0.3	3	$\gtrsim 0.66$	18.87 ± 0.05	3.2
(11705) 1998 GN7	1	20	2.99	2.03	5.3	3.8 ± 0.3	2	$\gtrsim 0.32$	16.65 ± 0.02	2.64
(12845) Crick	3	86	2.81	1.86	6.6	3.52 ± 0.05	2	$\gtrsim 0.21$	18.51 ± 0.04	2.79
(12895) Balbastre	3	128	2.03	1.07	8.7	3.8 ± 0.04	2	$\gtrsim 0.32$	17.02 ± 0.02	2.24
(13246) 1998 MJ33	4	222	2.53	1.57	6.9	14 ± 0.2	3	$\gtrsim 0.25$	17.48 ± 0.03	2.67
(14164) Hennigar	2	49	2.82	1.86	6.2	11.8 ± 0.2	2	$\gtrsim 0.88$	18.54 ± 0.04	2.94
(14197) 1998 XK72	4	161	3.02	2.06	5.7	10.7 ± 0.1	3	$\gtrsim 0.67$	18.17 ± 0.04	3.04
(14712) 2000 CO51	3	36	3.18	2.23	5.6	13.7 ± 0.2	2	$\gtrsim 0.42$	17.83 ± 0.03	3.01
(16228) 2000 EC39	4	123	3.6	2.65	5.3	6.2 ± 0.2	2	$\gtrsim 0.27$	19.17 ± 0.06	3.12
(20601) 1999 RD197	3	59	3.41	2.47	5.6	3.36 ± 0.04	3	$\gtrsim 0.24$	19.02 ± 0.05	2.64
(21705) Subinmin	3	65	2.87	1.91	5.6	3.46 ± 0.03	3	$\gtrsim 0.62$	18.91 ± 0.06	2.69
(25112) Mymeshkovych	3	76	2.94	1.98	5.7	10.1 ± 0.2	2	$\gtrsim 0.44$	19.06 ± 0.06	2.88
(25171) 1998 SX66	3	97	3.03	2.07	5.6	11.6 ± 0.2	3	$\gtrsim 0.5$	18.99 ± 0.06	2.92
(28509) 2000 CB92	2	23	2.27	1.3	6.9	5.04 ± 0.09	2	$\gtrsim 0.43$	18.28 ± 0.03	2.26
(32522) 2001 OE81	3	30	2.49	1.53	7.5	3.62 ± 0.01	3	$\gtrsim 0.26$	18.2 ± 0.03	2.38
(32553) 2001 QC27	3	30	3.53	2.57	4.3	4 ± 0.05	3	$\gtrsim 0.26$	18.35 ± 0.05	3.35
(33934) 2000 LA30	3	54	2.92	1.97	6.1	5.2 ± 0.1	2	$\gtrsim 0.67$	20.2 ± 0.1	2.39
(35005) 1979 MY3	4	72	2.83	1.88	6.6	7.24 ± 0.06	2	$\gtrsim 0.47$	19.27 ± 0.06	2.56
(36349) 2000 NZ23	4	104	2.73	1.77	6.7	6.7 ± 0.1	3	$\gtrsim 0.43$	19.01 ± 0.05	2.54
(36402) 2000 OT47	4	110	2.79	1.83	6.5	8.2 ± 0.05	3	$\gtrsim 0.57$	18.93 ± 0.05	2.54
(36524) 2000 QS80	3	81	2.5	1.54	7.1	4.26 ± 0.03	3	$\gtrsim 0.44$	18.32 ± 0.03	2.56
(44534) 1998 YZ9	4	144	2.16	1.21	9	22.5 ± 0.5	2	$\gtrsim 0.7$	18.61 ± 0.04	2.37
(45259) 2000 AF1	3	56	3.25	2.3	6.1	11.7 ± 0.2	3	$\gtrsim 0.85$	19.54 ± 0.07	2.94
(45601) 2000 DE5	3	33	3.08	2.12	4.9	3.38 ± 0.01	3	$\gtrsim 0.32$	18.63 ± 0.05	2.96
(46672) 1996 OA	2	37	3.33	2.37	5.3	3.55 ± 0.02	3	$\gtrsim 0.4$	19.08 ± 0.05	3.1
(47149) 1999 RX34	4	100	2.52	1.56	7	9.5 ± 0.09	3	$\gtrsim 0.49$	18.55 ± 0.04	2.13
(47154) 1999 RE141	3	64	2.89	1.94	6.1	5.2 ± 0.02	3	$\gtrsim 0.67$	19.71 ± 0.08	2.69
(48233) 2001 LY9	3	79	3.56	2.61	5.3	3.62 ± 0.02	3	$\gtrsim 0.7$	19.52 ± 0.07	3.17
(49766) 1999 WS	2	24	2.34	1.39	7.9	6.7 ± 0.1	2	$\gtrsim 0.76$	18.5 ± 0.04	2.14
(57394) 2001 RD84	4	52	2.21	1.24	7	6.74 ± 0.06	3	$\gtrsim 0.6$	18.29 ± 0.06	2.32
(57815) 2001 WV25	2	30	2.5	1.55	7.2	6 ± 0.08	2	$\gtrsim 0.34$	18.79 ± 0.04	2.35
(60527) 2000 EE43	3	59	2.97	2.02	6.5	6.01 ± 0.04	2	$\gtrsim 0.36$	19.08 ± 0.05	3.05
(61358) 2000 PK12	4	113	2.74	1.78	6.1	2.57 ± 0.02	2	$\gtrsim 0.28$	19.01 ± 0.05	2.54
(61378) 2000 PU28	3	103	2.88	1.92	6.2	4.69 ± 0.01	3	$\gtrsim 0.79$	19.84 ± 0.09	2.43
(63429) 2001 MH5	2	34	2.67	1.72	7.2	9.2 ± 0.2	3	$\gtrsim 0.78$	19.29 ± 0.06	2.31
(69802) 1998 RX15	2	18	3.01	2.05	5.8	5.3 ± 0.1	2	$\gtrsim 0.48$	19.47 ± 0.07	2.87
(71314) 2000 AW76	2	56	2.81	1.86	6.5	5.65 ± 0.08	3	$\gtrsim 0.81$	18.45 ± 0.05	2.85
(74421) 1999 AW24	3	58	2.86	1.91	6.7	3.66 ± 0.02	3	$\gtrsim 0.42$	18.98 ± 0.05	3.16
(77768) 2001 QM	3	36	3.2	2.24	4.6	7.1 ± 0.2	2	$\gtrsim 0.34$	18.77 ± 0.07	3.23
(77829) 2001 QO217	3	125	3.09	2.14	5.5	13.6 ± 0.3	3	$\gtrsim 0.62$	18.86 ± 0.06	3.2
(78296) 2002 PT53	2	23	3.14	2.18	5.3	5.3 ± 0.1	3	$\gtrsim 0.94$	19.22 ± 0.07	3.07
(78420) 2002 QU40	2	22	3.44	2.48	4.5	4.9 ± 0.05	2	$\gtrsim 1.11$	19.33 ± 0.07	3.07
(79721) 1998 SE112	3	44	2.84	1.89	6.7	10.2 ± 0.6	2	$\gtrsim 0.45$	20.2 ± 0.1	2.24
(87028) 2000 JA78	3	93	2.76	1.81	6.2	6.02 ± 0.09	2	$\gtrsim 0.57$	19.77 ± 0.08	2.35
(87988) 2000 TZ62	2	32	2.25	1.28	6.6	4.1 ± 0.2	2	$\gtrsim 0.42$	17.92 ± 0.05	2.62
(90896) 1997 CJ3	3	91	2.44	1.48	7.8	7.4 ± 0.2	2	$\gtrsim 0.45$	18.36 ± 0.04	2.67
(92519) 2000 NO27	4	186	2.46	1.5	6.8	3.08 ± 0.02	3	$\gtrsim 0.26$	18.48 ± 0.05	2.36
(93335) 2000 SK235	3	65	2.42	1.47	7.5	6.3 ± 0.1	3	$\gtrsim 0.9$	20 ± 0.1	2.55
(94653) 2001 WF67	3	92	2.13	1.18	9.4	4.8 ± 0.06	3	$\gtrsim 0.73$	19.17 ± 0.06	2.39
(95796) 2003 FM24	2	30	2.54	1.58	6.1	7.2 ± 0.2	2	$\gtrsim 0.45$	19.62 ± 0.08	2.39
(98993) 2001 DC36	2	46	2.75	1.79	6.4	3.22 ± 0.03	2	$\gtrsim 0.58$	19.6 ± 0.07	2.74
(101668) 1999 CR95[a]	4	178	2.82	1.87	6.1	16.54 ± 0.06	2	$\gtrsim 0.81$	18.79 ± 0.05	3.15
(105026) 2000 KX30	4	109	3.24	2.28	5	4.25 ± 0.02	3	$\gtrsim 0.73$	19.68 ± 0.08	3.16

Table 2 – *continued*

Designation	$N_{\rm nights}$	$N_{\rm im}$	r (au)	Δ (au)	α (°)	Period (h)	U	Amp (mag)	$\langle R_{\rm PTF}\rangle$ (mag)	a (au)
(116449) 2004 AU	4	124	2.61	1.65	6.5	15.3 ± 0.7	2	$\gtrsim 0.33$	18.24 ± 0.04	3.15
(118217) 1996 EO7	2	28	1.99	1.03	8.8	5.61 ± 0.09	2	$\gtrsim 1.06$	19.27 ± 0.06	2.33
(121532) 1999 UD40	2	20	2.88	1.92	5.7	2.25 ± 0.01	2	$\gtrsim 0.5$	19.48 ± 0.08	2.67
(124260) 2001 QK12	3	190	2.49	1.53	7	2.75 ± 0.01	2	$\gtrsim 0.62$	19.73 ± 0.08	2.37
(124374) 2001 QU152	2	51	2.26	1.3	8.1	9.7 ± 0.3	2	$\gtrsim 0.61$	19.33 ± 0.06	2.27
(124966) 2001 TH105	3	51	2.31	1.36	8.3	5.5 ± 0.04	2	$\gtrsim 0.65$	19.11 ± 0.05	2.43
(126334) 2002 AW152	4	53	2.42	1.47	7.7	3.51 ± 0.02	2	$\gtrsim 0.43$	19.26 ± 0.06	2.54
(126935) 2002 EN146	3	116	2.83	1.88	6.3	6.03 ± 0.05	3	$\gtrsim 0.88$	19.7 ± 0.08	2.63
(129100) 2004 XY4	2	57	2.65	1.69	6.5	6.8 ± 0.1	3	$\gtrsim 0.97$	19.51 ± 0.07	2.71
(192591) 1999 CE8	3	59	2.59	1.64	7.8	4.59 ± 0.03	3	$\gtrsim 0.36$	18.83 ± 0.04	3.15
(192665) 1999 RS181	3	73	2.69	1.73	6.4	5.45 ± 0.05	2	$\gtrsim 0.74$	20.2 ± 0.1	2.7
(195812) 2002 QL19	3	36	3.33	2.37	4.5	4.66 ± 0.03	3	$\gtrsim 0.71$	19.99 ± 0.1	3.04
(196214) 2003 BD37	2	36	2.34	1.38	7.5	6.8 ± 0.1	2	$\gtrsim 0.55$	19.16 ± 0.06	2.36
(197402) 2003 YN34	2	22	2.71	1.76	7.1	3.9 ± 0.02	2	$\gtrsim 0.93$	19.71 ± 0.08	3.14
(215701) 2003 YD121	3	49	3.31	2.35	4.4	6 ± 0.1	2	$\gtrsim 0.6$	19.71 ± 0.08	3.23
(230204) 2001 ST265	2	28	2.16	1.2	8.4	4.6 ± 0.1	2	$\gtrsim 0.66$	20.2 ± 0.1	2.43
(231051) 2005 GW60	2	29	3.3	2.36	5.8	9.4 ± 0.8	2	$\gtrsim 0.67$	20.2 ± 0.1	3.18
(231717) 1999 CK9	2	36	2.66	1.7	6.5	4.2 ± 0.1	2	$\gtrsim 0.57$	19.39 ± 0.07	3.12
(231927) 2001 DU30[a]	4	177	2.19	1.23	7.9	24.4 ± 0.1	2	$\gtrsim 0.72$	18.62 ± 0.05	2.76
(231958) 2001 PF28	2	46	2.89	1.93	5.6	4.5 ± 0.1	2	$\gtrsim 0.6$	19.11 ± 0.06	3.06
(283741) 2002 XH118	3	55	2.14	1.18	8.9	6.48 ± 0.02	3	$\gtrsim 1.09$	20.1 ± 0.1	2.33
2010 CA149	3	93	1.98	1.02	9.2	5.04 ± 0.03	2	$\gtrsim 0.71$	19.76 ± 0.09	2.32
2010 CV249	2	35	···	···	···	5.9 ± 0.2	2	$\gtrsim 0.51$	20.5 ± 0.1	3.26
P0007F	2	56	···	···	···	7.4 ± 0.3	2	$\gtrsim 0.93$	20.3 ± 0.1	···
P00095	2	39	···	···	···	3.26 ± 0.03	2	$\gtrsim 0.83$	20.6 ± 0.1	···
P000ZL	2	53	···	···	···	6.7 ± 0.2	2	$\gtrsim 0.73$	20.05 ± 0.1	···

Note. Columns: asteroids' designations, number of nights, number of images, geocentric (r) and heliocentric (Δ) distances, phase angle (α), rotation periods, period's reliability code, light-curve amplitude, mean magnitude and semimajor axis.
[a]A possible binary asteroid. The period is probably the orbital period of the satellite.

Table 3. Uncertain synodic rotation periods ($U = 1$) of 18 asteroids.

Designation	$N_{\rm nights}$	$N_{\rm im}$	r (au)	Δ (au)	α (°)	Period (h)	U	Amp (mag)	$\langle R_{\rm PTF}\rangle$ (mag)	a (au)
(9337) 1991 FO1	1	52	2.8	1.84	5.6	3.2 ± 0.1	1	$\gtrsim 0.26$	17.46 ± 0.02	2.86
(11027) Astaf'ev	4	106	2.32	1.37	8.4	4.87 ± 0.07	1	$\gtrsim 0.18$	17.75 ± 0.03	2.16
(13503) 1988 RH6	3	92	2.37	1.41	8.1	6.9 ± 0.1	1	$\gtrsim 0.23$	17.65 ± 0.03	2.25
(17293) 2743 P-L[a]	3	115	2.11	1.16	9.3	23.24 ± 0.07	1	$\gtrsim 0.43$	17.53 ± 0.02	2.39
(30338) 2000 JW29	4	145	2.15	1.19	8.2	39 ± 1	1	$\gtrsim 0.44$	17.82 ± 0.03	2.31
(31388) 1998 YL2	2	22	2.17	1.2	7.2	4.27 ± 0.03	1	$\gtrsim 0.3$	18.41 ± 0.04	2.38
(40791) 1999 TO33	3	64	2.82	1.87	6.8	3.133 ± 0.008	1	$\gtrsim 0.66$	19.09 ± 0.05	2.7
(47714) 2000 DS24	1	34	3.33	2.38	5.8	10 ± 2	1	$\gtrsim 0.57$	19.64 ± 0.07	2.98
(56682) 2000 LA9	3	125	2.22	1.26	7.8	2.54 ± 0.04	1	$\gtrsim 0.15$	18.05 ± 0.05	2.33
(113117) 2002 RF80	2	24	2.76	1.81	6.4	12.3 ± 0.2	1	$\gtrsim 0.72$	19.3 ± 0.07	3.2
(115359) 2003 SA250	1	36	3.03	2.09	6.4	5.4 ± 0.08	1	$\gtrsim 1.46$	19.6 ± 0.08	2.94
(129691) 1998 SH16	3	86	2.91	1.96	5.9	17.1 ± 0.8	1	$\gtrsim 0.62$	20.4 ± 0.1	2.87
(133528) Ceragioli	3	79	3.02	2.08	6.6	3.06 ± 0.04	1	$\gtrsim 0.52$	20.1 ± 0.1	2.86
(197388) 2003 YN11	3	108	2.98	2.02	5.8	14.9 ± 0.9	1	$\gtrsim 0.83$	20.2 ± 0.1	3.15
(228255) 1999 ET7	3	45	2.88	1.93	6.2	4.2 ± 0.1	1	$\gtrsim 0.54$	20.3 ± 0.1	3.16
2003 WP9	3	98	2.9	1.94	6	6.76 ± 0.05	1	$\gtrsim 0.83$	20.2 ± 0.1	3.02
2007 EZ184	3	54	···	···	···	2 ± 0.03	1	$\gtrsim 0.52$	20.3 ± 0.1	2.27
P000K7	2	44	···	···	···	3.23 ± 0.02	1	$\gtrsim 0.47$	19.4 ± 0.06	···

Note. Columns like Table 2.
[a]A possible binary asteroid. The period is probably the orbital period of the satellite.

Dust and gas ejection from minor planets can be the result of cometary activity or a collisional event. Such objects can be detected as moving sources, with a signature extended point spread function. The large sample of asteroids visible in PTF images is being used to search for gas and dust around minor planets and to probe their ice content, as well as to study the dynamical history of the main belt (Waszczak, Ofek & Polishook 2011a; Waszczak et al. 2011b).

Table 4. Lower limits on the synodic rotation periods of 67 asteroids.

Designation	$N_{\rm nights}$	$N_{\rm im}$	r (au)	Δ (au)	α (°)	Period (h)	Amp (mag)	$\langle R_{\rm PTF}\rangle$ (mag)	a (au)
(1516) Henry	2	23	2.48	1.51	6.3	$\gtrsim 5$	$\gtrsim 0.03$	15.13 ± 0.02	2.62
(1788) Kiess	2	37	3.61	2.65	4.9	$\gtrsim 9$	$\gtrsim 0.8$	17.29 ± 0.03	3.11
(3111) Misuzu	1	38	2.29	1.33	7.2	$\gtrsim 9$	$\gtrsim 0.18$	16.47 ± 0.02	2.22
(4741) Leskov	3	46	3.68	2.74	5.2	$\gtrsim 9$	$\gtrsim 0.1$	17.85 ± 0.03	3.22
(5807) Mshatka	3	49	3.37	2.42	5.4	$\gtrsim 8.6$	$\gtrsim 0.3$	18.06 ± 0.04	3.05

Note. Columns: asteroids' designations, number of nights, number of images, geocentric (r) and heliocentric (Δ) distances, phase angle (α), limit on the rotation period, light-curve amplitude, mean magnitude and semimajor axis. This table is published in its entirety as Supporting Information with the electronic version of the article. A portion of the full table is shown here for guidance regarding its form and content.

Table 5. Lower limits on the amplitude of 451 asteroids.

Designation	$N_{\rm nights}$	$N_{\rm im}$	r (au)	Δ (au)	α (°)	Amp (mag)	$\langle R_{\rm PTF}\rangle$ (mag)	a (au)
(625) Xenia	3	57	3.2	2.25	5.8	$\gtrsim 0$	14.49 ± 0.02	2.65
(1079) Mimosa	2	14	2.8	1.84	5.77	$\gtrsim 0.1$	14.95 ± 0.04	2.87
(3679) Condruses	2	23	2.34	1.38	7.65	$\gtrsim 0.1$	15.13 ± 0.02	2.2
(5179) Takeshima	2	37	2.22	1.26	7.21	$\gtrsim 0.1$	17.29 ± 0.03	2.31
(6916) Lewispearce	2	57	3.2	2.25	5.34	$\gtrsim 0.3$	15.42 ± 0.02	2.84

Note. Columns: asteroids' designations, number of nights, number of images, geocentric (r) and heliocentric (Δ) distances, phase angle (α), lower limit on the light-curve amplitude, mean magnitude and semimajor axis. This table is published in its entirety as Supporting Information with the electronic version of the article. A portion of the full table is shown here for guidance regarding its form and content.

PTF photometry is calibrated to a precision of better than 0.04 mag, even outside SDSS footprints (Ofek et al. 2012) and it provides accurate magnitudes of asteroids in the visible range. Therefore, PTF data could be combined with the archive of NASA's *Wide-field Infrared Survey Explorer* (*WISE*) telescope. During 9 months of full cryogenic operations, the *WISE* telescope observed about 200 000 asteroids in the near-IR (Mainzer et al. 2010); most of these lack accurate absolute magnitudes in visible wavelengths (Masiero et al. 2011). Therefore, the two data sets combined could improve the size measurements for a significant number of asteroids.

Binary asteroids are difficult to identify because eclipses/occultations repeat themselves only after long periods (tens of hours) and last for short times. Our survey can find a large number of binary asteroids through the detection of eclipses and occultations. This can provide the statistics on binary asteroids as a function of their physical parameters. It is estimated that approximately 16 per cent of near-Earth asteroids are binaries (Margot et al. 2002). Applying this ratio to main-belt asteroids, and assuming that eclipses/occultations can be detected during 10–30 per cent of the orbital period (Pravec et al. 2006), it can be estimated that out of $\approx$100 asteroids measured photometrically by the PTF, between two and five objects will register an eclipse or an occultation. This ratio is supported by our findings of three binary candidates. Enlarging the sample could determine the number of binaries among main-belt asteroids. This has important implications because any difference between the fraction of binaries among main-belt asteroids and near-Earth asteroids can constrain binary formation mechanisms and their dependencies on the asteroid environment.

The photometry of asteroids measured by PTF could also be used to derive asteroid shapes and rotational states (sidereal period and spin axis). This is done by the light-curve inversion method that uses brightness measurements obtained over a wide range of viewing geometries during a few apparitions to build a complete model of the asteroid (e.g. Kaasalainen & Torppa 2001; Hanuš et al. 2011). PTF will revisit many asteroids during a few apparitions, and so the light-curve inversion method could be applied to a large sample of small-sized asteroids, thus contributing to the study of asteroid spins and shapes.

ACKNOWLEDGMENTS

We thank the referee for useful comments. This paper is based on observations obtained with the Samuel Oschin Telescope as part of the Palomar Transient Factory project, a scientific collaboration between the California Institute of Technology, Columbia University, Las Cumbres Observatory, the Lawrence Berkeley National Laboratory, the National Energy Research Scientific Computing Center, the University of Oxford and the Weizmann Institute of Science. The Weizmann PTF partnership is funded in part by grants from the Israeli Science Foundation (ISF) to AG-Y. PTF Collaborative work between the Weizmann and Caltech groups is supported by the Binational Science Foundation (BSF) via grants to SRK and AG-Y. DPol further acknowledges support from the Benoziyo Center for Astrophysics and the Yeda-Sela Center at WIS. SRK and his group are partially supported by the NSF grant AST–0507734. SBC wishes to acknowledge generous support from Gary and Cynthia Bengier, the Richard and Rhoda Goldman Fund, NASA/*Swift* grant NNX10AI21G, NASA/*Fermi* grant NNX1OA057G and National Science Foundation (NSF) grant AST–0908886.

Table 6. All measurements of the detected asteroids.

Designation	Field	CCD	JD (d)	RA (°)	Dec. (°)	R_{PTF} (mag)	AM	Background (counts)	⟨FWHM⟩ (arcsec)	r (au)	Δ (au)	α (°)	a (au)	e	i (°)
(625) Xenia	110001	01	245 5239.7052872	127.88457	19.86213	14.4627 ± 0.0244	1.15	1165.51	2.18	3.202	2.249	5.464	2.647	0.225	12.057
(625) Xenia	110002	07	245 5239.7070572	127.88419	19.86229	14.5167 ± 0.0352	1.14	1120.50	2.15	3.202	2.249	5.465	2.647	0.225	12.057
(625) Xenia	110001	01	245 5239.7176472	127.88195	19.86330	14.4548 ± 0.0245	1.12	1322.92	2.16	3.202	2.249	5.469	2.647	0.225	12.057
(625) Xenia	110002	07	245 5239.7194372	127.88157	19.86346	14.5010 ± 0.0352	1.11	1134.90	2.31	3.202	2.249	5.469	2.647	0.225	12.057
(625) Xenia	110001	01	245 5239.7300672	127.87931	19.86446	14.4486 ± 0.0249	1.09	2019.15	3.18	3.202	2.249	5.473	2.647	0.225	12.057

Note. Columns: asteroids' designations, PTF's field and CCD, JD, RA, Dec., calibrated magnitude, air mass, image's background count and FWHM. The last six parameters are given only for objects with known orbital parameters: geocentric (r) and heliocentric (Δ) distances, phase angle (α), semimajor axis, eccentricity and inclination. This table is published in its entirety as Supporting Information with the electronic version of the article. A portion of the full table is shown here for guidance regarding its form and content.

REFERENCES

Agüeros M. A. et al., 2011, ApJ, 740, 110
Arcavi I. et al., 2010, ApJ, 721, 777
Bendjoya P., Zappalà V., 2002, in Bottke W. F., Jr, Cellino A., Paolicchi P., Binzel R. P., eds, Asteroids III. Univ. Arizona Press, Tucson, p. 613
Bertin E., Arnouts S., 1996, A&AS, 117, 393
Bowell E., Hapke B., Domingue D., Lumme K., Peltoniemi J., Harris A. W., 1989, in Binzel R. P., Gehrels T., Matthews M. S., eds, Asteroids II. Univ. Arizona Press, Tucson, p. 524
Davis D. R., Durda D. D., Marzari F., Campo Bagatin A., Gil-Hutton R., 2002, in Bottke W. F., Jr, Cellino A., Paolicchi P., Binzel R. P., eds, Asteroids III. Univ. Arizona Press, Tucson, p. 545
Galad A., Kornos L., Gajdos S., 2009, Minor Planet Bull., 36, 13
Gnat O., Sari R., 2010, ApJ, 719, 1602
Grav T., Jedicke R., Denneau L., Chesley S., Holman M. J., Spahr T. B., 2011, PASP, 123, 423
Grillmair C. J. et al., 2010, in Mizumoto Y., Morita K., Ohishi M., eds, ASP Conf. Ser. Vol. 434, Astronomical Data Analysis Software and Systems XIX. Astron. Soc. Pac., San Francisco, p. 28
Hanuš J. et al., 2011, A&A, 530, A134
Harris A. W. et al., 1989, Icarus, 77, 171
Høg E. et al., 2000, A&A, 355, L27
Honeycutt R. K., 1992, PASP, 104, 435
Ivezić Ž. et al., 2001, AJ, 122, 2749
Kaasalainen M., Torppa J., 2001, Icarus, 153, 24
Kron R. G., 1980, ApJS, 43, 305
Lagerkvist C. I., Magnusson P., 1990, A&AS, 86, 119
Law N. M. et al., 2009, PASP, 121, 1395
Levitan D. et al., 2011, ApJ, 739, 68
Mainzer A. K. et al., 2010, BAAS, 42, 1016
Margot J. L., Nolan M. C., Benner L. A. M., Ostro S. J., Jurgens R. F., Giorgini J. D., Slade M. A., Campbell D. B., 2002, Sci, 296, 1445
Masiero J., Jedicke R., Ďurech J., Gwyn S., Denneau L., Larsen J., 2009, Icarus, 204, 145
Masiero J. R. et al., 2011, ApJ, 741, 68
Ofek E. O., 2012, ApJ, preprint (arXiv:1202.1538)
Ofek E. O., Frail D. A., Breslauer B., Kulkarni S. R., Chandra P., Gal-Yam A., Kasliwal M. M., Gehrels N., 2011, ApJ, 740, 65
Ofek E. O. et al., 2012, PASP, 124, 62
Polishook D., Brosch N., 2009, Icarus, 199, 319
Polishook D., Brosch N., Prialnik D., 2011, Icarus, 212, 167
Pravec P., Harris A. W., 2000, Icarus, 148, 12
Pravec P. et al., 2006, Icarus, 181, 63
Pravec P. et al., 2008, Icarus, 197, 497
Pravec P. et al., 2010, Nat, 466, 1085
Rahmer G., Smith R., Velur V., Hale D., Law N., Bui K., Petrie H., Dekany R., 2008, in McLean I. S., Casali M. M., eds, Proc. SPIE Vol. 7014, Ground-based and Airborne Instrumentation for Astronomy II. SPIE, Bellingham, 70144Y
Rau A. et al., 2009, PASP, 121, 1334
Rubincam D. P., 2000, Icarus, 148, 2
van Eyken J. C. et al., 2011, AJ, 142, 60
Vokrouhlický D., Čapek D., 2002, Icarus, 159, 449
Vokrouhlický D., Nesvorný D., 2008, AJ, 136, 280
Warner B. D., Harris A. W., Pravec P., 2009, Icarus, 202, 134
Waszczak A., Ofek E. O., Polishook D., 2011a, Central Bureau Electronic Telegrams, 2823, 1
Waszczak A., Ofek E. O., Kulkarni S., Polishook D., 2011b, in EPSC-DPS Joint Meeting 2011
York D. G. et al., 2000, AJ, 120, 1579

SUPPORTING INFORMATION

Additional Supporting Information may be found in the online version of this article.

Table 4. Lower limits on the synodic rotation periods of 67 asteroids.
Table 5. Lower limits on the amplitude of 451 asteroids.
Table 6. All measurements of the detected asteroids.
Figure 11. Set of light curves with lower limits on the rotation periods.

This paper has been typeset from a TEX/LATEX file prepared by the author.